2nd Advanced Optical Metrology Compendium

Advanced Optical Metrology

Geoscience | Corrosion | Particles | Additive
Manufacturing: Metallurgy, Cut Analysis & Porosity

EVIDENT
OLYMPUS

WILEY

The latest eBook from Advanced Optical Metrology. Download for free.

This compendium includes a collection of optical metrology papers, a repository of teaching materials, and instructions on how to publish scientific achievements.

With the aim of improving communication between fundamental research and industrial applications in the field of optical metrology we have collected and organized existing information and made it more accessible and useful for researchers and practitioners.

EVIDENT
OLYMPUS

WILEY

Morphological Control Over Gel Structures of Mixed Semiconductor-Metal Nanoparticle Gel Networks with Multivalent Cations

Marina Rosebrock, Dániel Zámbó,* Pascal Rusch, Rebecca T. Graf, Denis Pluta, Hadir Borg, Dirk Dorfs, and Nadja C. Bigall*

In this work, the influence of two different types of cations on the gel formation and structure of mixed gel networks comprised of semiconductor (namely CdSe/CdS nanorods NR) and Au nanoparticles (NP) as well as on the respective monocomponent gels is investigated. Heteroassemblies built from colloidal building blocks are usually prepared by ligand removal or cross-linking, thus, both the surface chemistry and the destabilising agent play an essential role in the gelation process. Due to the diversity of the composition, morphology, and optical properties of the nanoparticles, a versatile route to fabricate functional heteroassemblies is of great demand. In the present work, the optics, morphology, and gelation mechanism of pure semiconductor and noble metal as well as their mixed nanoparticle gel networks are revealed. The influence of the gelation agents (bivalent and trivalent cations) on the structure-property correlation is elucidated by photoluminescence, X-ray photoelectron spectroscopy, and electron microscopy measurements. The selection of cations drastically influences the nano- and microstructure of the prepared gel network structures driven by the affinity of the cations to the ligands and the nanoparticle surface. This gelation technique provides a new platform to control the formation of porous assemblies based on semiconductor and metal nanoparticles.

1. Introduction

Present and past studies of nanoparticles assemblies in the form of macroscopic network structures (that is, nanocrystal-based hydrogels and aerogels) via bottom-up approach focus on the properties of various materials,[1–6] different material combinations,[7–15] shape-dependent properties[16] and applications[17–20]

by utilizing diverse gelation agents.[21,22] The main aspect being, that interparticle connections essentially govern the properties in nanoparticle assemblies, thus, the control over nanocrystal connections is the main tool toward tailored gel structures. Manifold gelation techniques have been explored in the recent decade: via addition of oxidative agents,[3,5] cryogelation,[23,24] ion-induced,[25–28] or via light irradiation.[6,22,29] All gelation methods are based on the concept of overcoming the interparticle repulsion forces in a stable colloidal solution of nanocrystals facilitating their controlled assembly. The resulting structures are as different as their methods, but overall they still deliver structures with large surface areas, low densities, high and open porosity. These properties unite all these structures, even if they differ greatly in their composition and the interaction between the building blocks. Especially in case of nanoparticle assemblies consisting of two or more different components (in the following named heteroassemblies), the connection itself between the particles has a great impact on the optical properties evolving in the gel networks, e.g., spatial separation of photoexcited charge carriers.[30–33]

In the present work, we give an insight into the importance of choosing the most suitable gelation agent for specific purposes requiring different gel morphologies. As recent studies have mostly dealt with ion-induced gelation of

M. Rosebrock, P. Rusch, R. T. Graf, D. Pluta, H. Borg, D. Dorfs,
N. C. Bigall
Institute of Physical Chemistry and Electrochemistry
Leibniz Universität Hannover
30167 Hanover, Germany
E-mail: nadja.bigall@pci.uni-hannover.de

The ORCID identification number(s) for the author(s) of this article can be found under https://doi.org/10.1002/smll.202206818.

M. Rosebrock, H. Borg, D. Dorfs, N. C. Bigall
Cluster of Excellence PhoenixD (Photonics, Optics and
Engineering – Innovation Across Disciplines)
Leibniz Universität Hannover
30167 Hanover, Germany

D. Zámbó
Institute of Technical Physics and Materials Science
Centre for Energy Research
Budapest 1121, Hungary
E-mail: daniel.zambo@ek-cer.hu

R. T. Graf, D. Pluta, D. Dorfs, N. C. Bigall
Laboratory for Nano and Quantum Engineering
Leibniz Universität Hannover
30167 Hanover, Germany

**ADVANCED
SCIENCE NEWS**

www.advancedsciencenews.com

NANO · MICRO

small

www.small-journal.com

single-origin materials (in the following named homoparticle assembly) or mixed noble metals,[26,27,34] this work compares the influence of bi- (Ca^{2+}, Ba^{2+}) and trivalent (Y^{3+}, Yb^{3+}) cations on the structure and property of nanoparticle gel networks with respect to heteroassemblies and derives a possible mechanism based on the results, which previous work has not included. The gelation of the building blocks is initiated in aqueous medium and at room temperature by introducing the respective salt solutions as external trigger. Beside the characterization of pure semiconductor (CdSe/CdS) or noble metal (Au and Pt) gel networks, heteroassemblies also are investigated in special regard of their morphology and optical properties.

The presence of noble metal nanocrystals within the semiconductor gel network can enable indirect optical characterization techniques delivering information about the interparticle contact.[31] In the present study, a direct effect of the gel formation on NR-NP contact is monitored based on the charge carrier formation upon irradiation and their separation within the NRs and electron extraction by the noble metal emerging in the structures.

Moreover, we provide a fast and easy-to-adapt approach to build up homogeneous mixed network structures. The concept enables the synthesis of the desired nanocrystals with tailored properties prior to their assembly into porous, functional gel structures. Since the connection between the building blocks plays a crucial role in the appearance and extent of synergistic properties, our aim is to support the selection of the destabilizing cation and to provide a low-cost and reproducible

synthesis pathway towards homo- and heteroparticle (mixed NRs with NPs) assemblies.

We found that the selection of cations (i.e., bi- or trivalent ones) drastically influences the nano- and microstructure of the prepared gel networks: while bivalent cations (Ca^{2+}, Ba^{2+}) connect the particles leading to a preferential side-by-side linkage of the elongated building blocks (i.e., NRs), trivalent cations (Y^{3+}, Yb^{3+}) tend to form tip-to-tip connected NR networks (see **Scheme 1**).

As we pointed out recently[5,27,31,35] the way how the building blocks interact in the gel network is of central importance regarding their structural and optical properties. Furthermore, the presence of noble metal particles in the semiconductor-based gels facilitates the charge carrier separation (electron extraction) from the CdSe/CdS NRs to the Au nanoparticles which might pave the way toward novel, e. g., optoelectronic or photoelectronic applications.

2. Results and Discussion

Semiconductor and noble metal nanoparticles are synthesized in organic medium and later transferred to aqueous solutions for gelation experiments (see Figure S1, Supporting Information, which shows the morphology, extinction and photoluminescence spectra of the building blocks' solution). The surface of all particles is grafted with 3-mercaptopropionic acid (MPA) ligands, and the colloidal solutions are stabilized in a basic aqueous medium (0.01 M KOH) leading to the deprotonation of
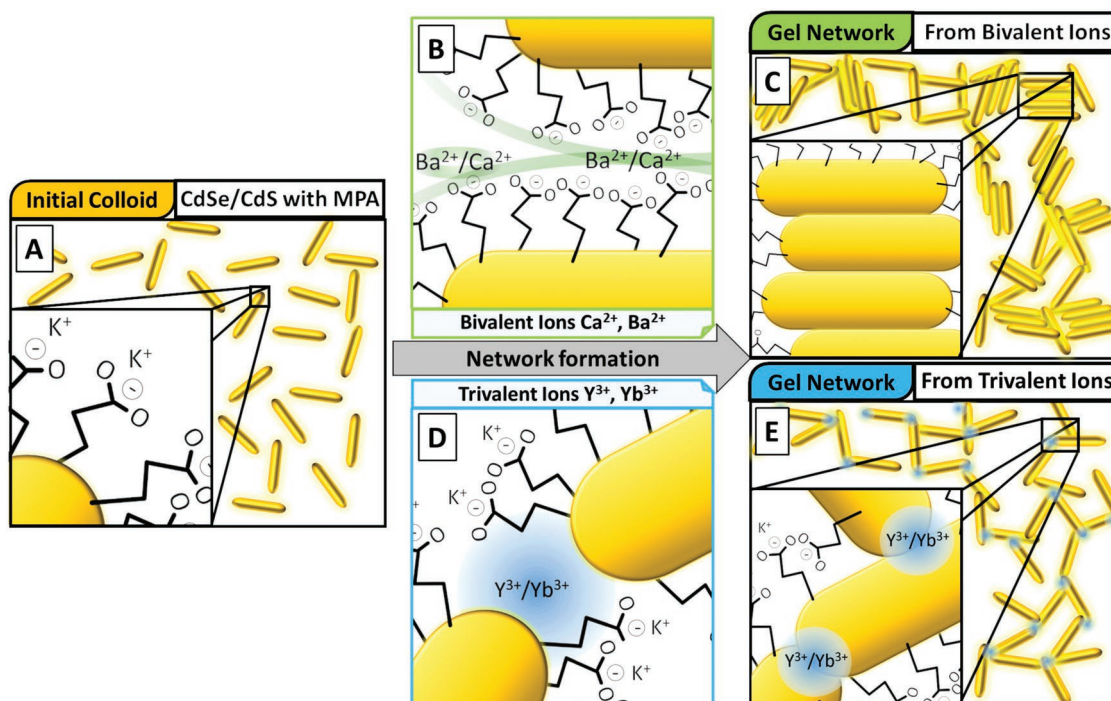
Scheme 1. Schematic representation showing the original, A) MPA-capped NRs and their different assembly preferences, namely B,C) side-by-side and D,E) tip-to-tip connection of the nanoparticle gel networks initialized by bi- and trivalent cations, respectively. These model system consist of soley CdSe/CdS NRs (Au NPs are not present in the system).

ADVANCED
SCIENCE NEWS
www.advancedsciencenews.com

NANO · MICRO
small
www.small-journal.com

the carboxylic acid groups of the surface attached MPA. These charged ligands prevent the nanoparticles from agglomeration due to repulsive electrostatic forces. Introduced ions interact with the nanoparticle surface and their charged ligands.[36] Triggering the colloidal destabilization, hence, the nanoparticles are able to get in contact and build up network structures.

Figure 1 gives an overview about the structural diversity of the NR networks from the nanoscopic point of view. Figure 1A,B shows that a porous network can be formed in both cases. At the nanoscopic level, however, we find significant differences in terms of the interconnections between the building blocks. Figure 1C–F shows comparative transmission electron microscopy (TEM) micrographs for all applied gelating ions. In Figure 1C,E, gelled with barium and calcium ions, the overall structure is dominated by side-by-side arrangement of the building blocks to form aggregates which are further connected to form a network. These networks are assembled randomly from all available buildings blocks and the building blocks retain their original shapes and properties. The lower magnification insets show a porous but significantly less branched structure compared to trivalent ion-induced structures in Figure 1D,F. Here, in case of trivalent ion-induced networks, we can observe a mainly tip-to-tip connected hyperbranched network structure which is more porous and open. A roughness of the gelled NRs can be observed in the TEM micrographs in case of Y^{3+} and Yb^{3+} indicating a ligand removal and etching process (see Figure 1D,F) on the nanoparticle surfaces. Removed ligands can be found in the supernatant after addition of the salt-solution to the initial nanoparticle colloids.[27] These rough surfaces will also have an impact on the fluorescence behavior which is discussed in detail (**Figure 2**) later.

Scheme 1 illustrates the suggested process of gel network formation triggered via the addition of the bivalent or trivalent cations, where the mechanism for trivalent ion-induced gelation is suggested by Zámbó et al.[27] Panel A represents the colloidal solution of pure CdSe/CdS NRs with deprotonated MPA ligands on the surface. The upper row in Scheme 1 (with green frame, panel (B) and (C)) depicts the proposed mechanism of the ion-induced gelation initialized by bivalent ions (namely Ca^{2+} or Ba^{2+} in the form of chloride salts). After the addition of the ionic solution to the stable colloid, an electrostatic interaction between the cationic component and the carboxylic acid group of MPA, more precisely between oxygen and Ca^{2+}/Ba^{2+}, can take place. Due to the bivalency of Ca^{2+}/Ba^{2+}, various connections can be proposed: i) the ions can bridge two particles across their ligands and ii) the ion can be located between the carboxylic acid group and sulfur atoms of the nanoparticle surface.[36] It has to be noted, however, that the latter case is thermodynamically less favorable,[36] thus, the interaction between COO⁻ groups and the cations might dominate the process. Due to the rod-like shape of the CdSe/CdS nanoparticles and the consequent curved tip region, the ligand coverage at the side region is expected to be significantly higher than at the tips. In addition, one tip of the rods has a sulfur-rich surface,[37] so MPA coverage is lower at this location. Consequently, the concentration of the ions attached to the ligands is higher at the side regions leading to a more dominant screening of the stabilizing charges at the sides. It results in the pre-formation and aggregation of NRs in solution (solution get turbid), which lead to a network structure consisting of more side-by-side arranged NR clusters in macroscopic assemblies (hydrogel). Importantly, during washing with large volume of ultrapure water, most bivalent ions can be eliminated from the assembled structure. This is supported by our findings derived from scanning electron microscopy with energy dispersive x-ray spectroscopy (SEM-EDXS) (see Figures S29 and S30, Supporting Information) and X-ray photoelectron spectroscopy (XPS) (see **Figure 3**) analysis, where bivalent ionic species are not detectable in our resulting purified gel networks of pure NRs. After the purification process, hydrogels are still intact which is an indication for crystal-to-crystal contacts between individual NRs.

Differently to the bivalent ions, trivalent ones remain in the structure and can be detected even after excessive washing and drying, which indicates their high affinity towards the NR surface. All measured samples contain measurable amounts of trivalent ions within the washed network structures (see Figures S29 and S30, Supporting Information). These findings are in agreement with our recent study.[27] In detail, for Y^{3+} and Yb^{3+} also a different morphology is found, namely, a network from mainly tip-to-tip connected NR (see blue frame, Scheme 1D,E). As we have shown earlier for similar seeded rod gel systems, as a gelation mechanism, a chemical ligand removal on the surface on the nanoparticles is anticipated.[27] This is supported by the higher resolution TEM micrographs (Figure 1D,F), where the surfaces of the NRs become visibly rough. The roughness in trivalent ion-gelled networks can be explained by different kinetics for ligand removal. We assume a faster ligand removal at the tips and a slower etching process for the side regions of NRs after the NR-NR connections are already formed. In case of lower concentration (1 mM) of trivalent ions, we can observe network formations (which are, however, much more fragile than with higher ionic concentrations) with much smoother side-regions of the NRs.[27] This implies, that the formation of the NR-NR connections takes place rapidly, that is followed by the etching of the gel surface in a second step. The tip-to-tip connection is also known for anisotropic nanoparticles, which are gelled with hydrogen peroxide.[5] Here, two effects have an influence of the resulting structures: i) due to the surface chemistry, crystal facets of nanoparticles at the tips (namely ⟨001⟩) are more reactive and have an increased surface energy[38] which makes them preferred for ligand removal. This can be described as facet-dependent removal, which takes place more favorably at the NR tips. ii) The second effect is the accessibility of ligands on the tips as a consequence of the curvature. Due to the shape of the tip and the resulting angle of the attached ligands, the access of the cations to the surface of the NR is less hindered.

The combination of the semiconductor NR and gold NP colloids prior to gelation leads to homogeneously distributed mixed network structures (see **Figure 4**). Nanorod connections are not influenced by the introduction of the Au, even if the Au NP concentration is high (particle ratio of NR:NP = 1:2), thus, similar side-by-side or tip-to-tip connected networks are formed as for pure NRs. NPs attach randomly to the NR backbone network without forming isolated nanoparticle aggregates.

For the gelation of pure spherical noble metal nanoparticles (see **Figure 5**), different ions induce a significant effect on the
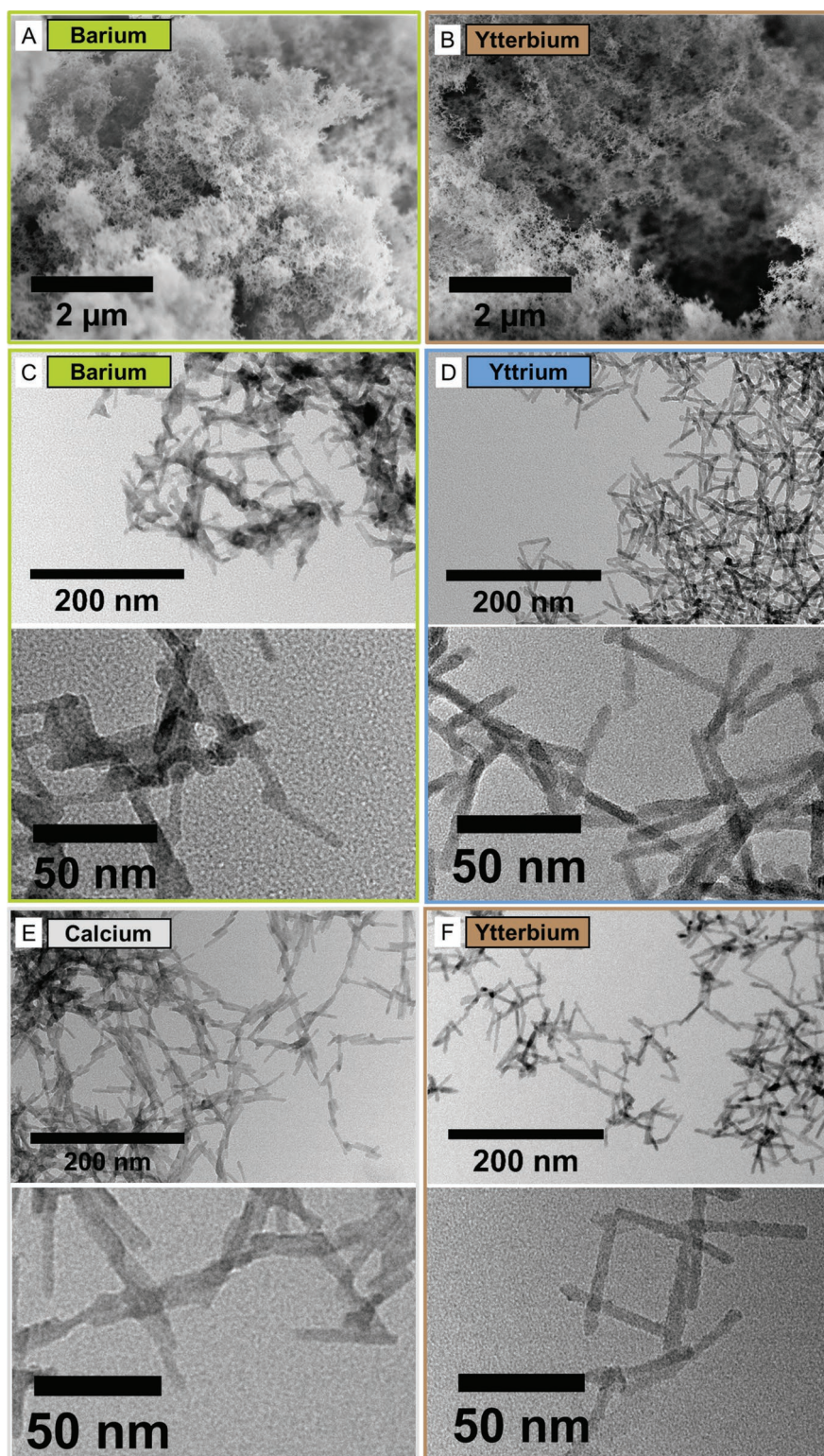
Figure 1. A) SEM micrographs from CdSe/CdS aerogel gelled with with Ba^{2+} and B) CdSe/CdS aerogel gelled with Yb^{3+}, which show a similar and porous structure. C–F) TEM micrographs of CdSe/CdS nanoparticle networks synthesized with different ions. Bivalent ion-gelled networks (C) and (E) show mostly side-by-side and trivalent ion-gelled networks (D) and (F) show a structure dominated by tip-to-tip arrangement of the particles.

structural properties of the Au gels. For bivalent cations, a dense and fused network structure is obtained and the particles lose their original morphology (Figure 5A,B) in contrast to trivalent cations (Figure 5C,D), where the Au NPs are also
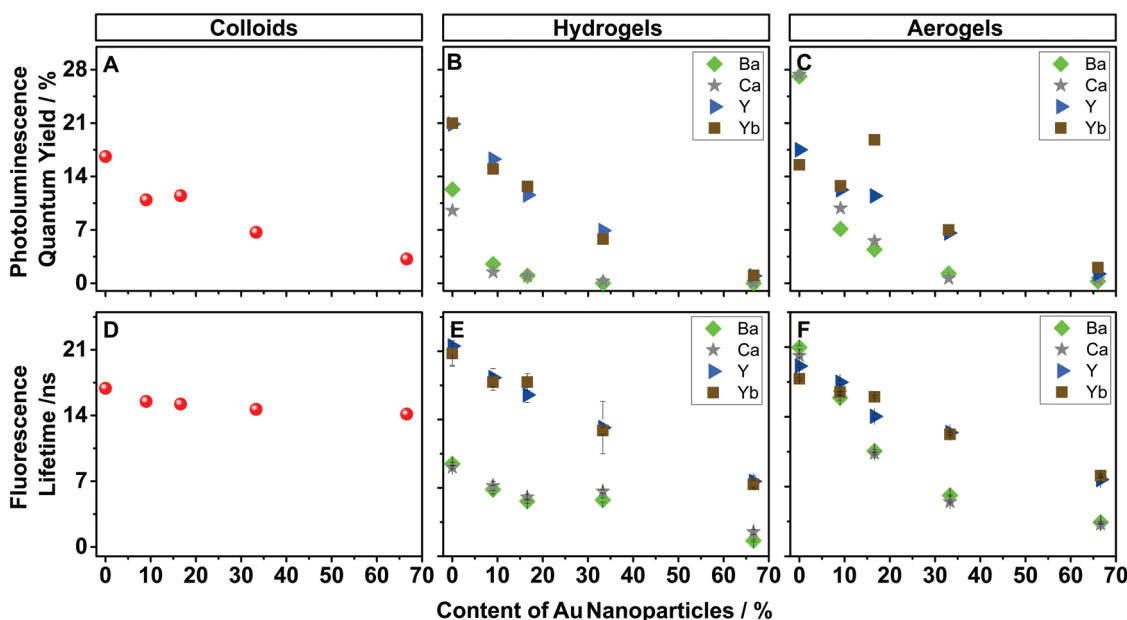
Figure 2. Fluorescence spectroscopy results on colloidal mixtures, hydrogels, and aerogels containing CdSe/CdS NRs and Au nanoparticles: A–C) photoluminescence quantum yield and D–F) fluorescence lifetime measurements. Hydrogels and aerogels are compared regarding the different gelation agents (Ca^{2+}, Ba^{2+}, Y^{3+}, and Yb^{3+}). Error bars in case of FLT values represent the error from the biexponential fitting of the decay curves.

partly connected but less fused. This manifests in the visual appearance of the macroscopic gels as well (see Figures S7 and S8, Supporting Information): bivalent ion-induced networks are less voluminous than trivalent ion-induced ones. These effects
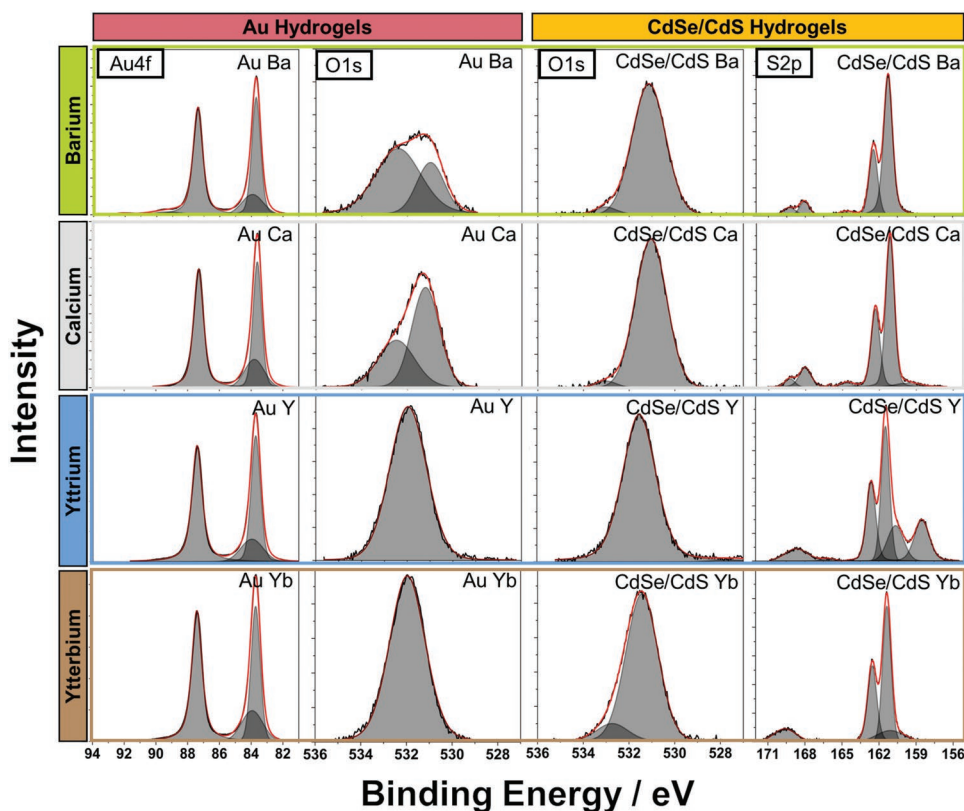

Figure 3. XPS spectra in the energy range of Au4f, O1s, and S2p orbitals. Comparison of pure Au and NR network structures obtained by ion-induced gelation with Ba^{2+}, Ca^{2+}, Y^{3+}, and Yb^{3+} (from their corresponding chlorides). Interaction of bivalent ions with NR surface does not take place, while it can be obtained for trivalent ions.
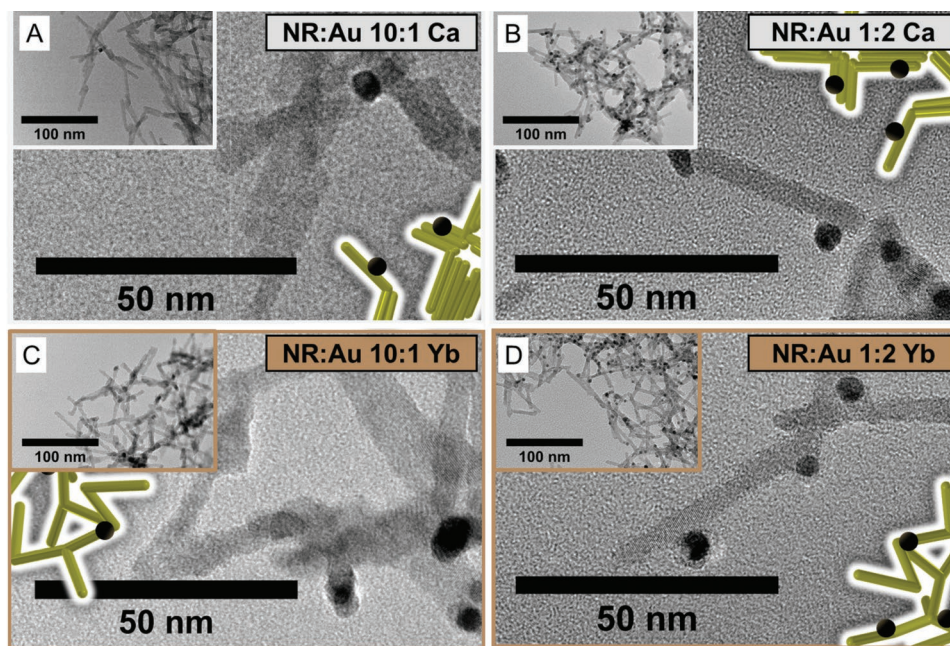
**ADVANCED
SCIENCE NEWS**

www.advancedsciencenews.com

NANO · MICRO

small

www.small-journal.com

Figure 4. TEM micrographs of selected CdSe/CdS:Au nanoparticle networks synthesized with A,B) Ca^{2+} ions, and with C,D) Yb^{3+} ions. All insets show lower magnification images to see the overall nanoscopic structures.

of fused nanoparticles could be attributed to the electronic properties of gold, which is more electron rich and has a higher affinity to the cationic species (bi- and trivalent). Residual amount of cations can be observed in the gold gels (see XPS studies Figure 3): Here, Au hydrogels and aerogels contain more trivalent cations than bivalent ones, thus, the valency of the investigated cations (as well as the ionic radius) has a direct

impact on their accumulation at the surface and hence on the nanoscopic properties of the pure noble metal gels. In case of higher amounts of Au NPs within the network, Ca (and a low amount of Ba) can be detected. This implies that bivalent ions are stronger attached to the noble metal surface. It can be concluded that the proposed mechanisms of electrostatic screening (dominating for bivalent cations) and ligand removal
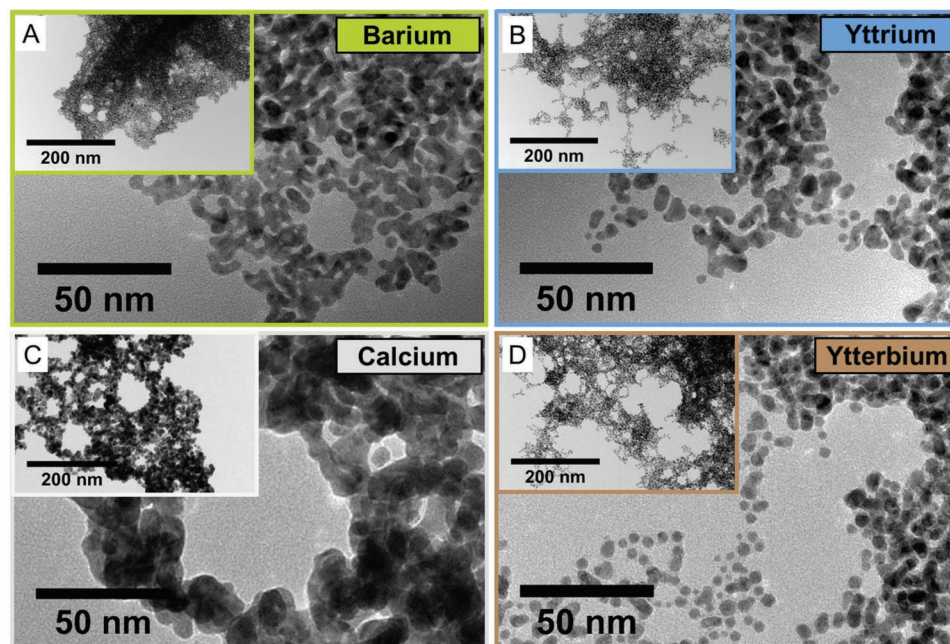

Figure 5. TEM micrographs of Au nanoparticle aerogel networks synthesized with A) Ba^{2+}, B) Ca^{2+}, C) Y^{3+}, and D) Yb^{3+}. Gel networks from bivalent ions tend to have a more fused structure compared to those from trivalent ions.

**ADVANCED
SCIENCE NEWS**

www.advancedsciencenews.com

**NANO · MICRO
small**

www.small-journal.com

(dominating for trivalent cations)[39] compete in the gel formation, however, the in-depth understanding of this complex process requires further focused investigations in the future.

In Figure 3, the relevant elemental regions in binding energy measured by XPS after cleaning and washing of the hydrogel samples. Here, the typical energy regions of S2p, O1s, and Au4f for pure Au networks and pure NR networks gelled with different ions (Ba^{2+}, Ca^{2+}, Y^{3+}, and Yb^{3+} from their corresponding chlorides) are shown in high resolution.

As seen for pure Au networks, the characteristics of all Au4f signals show great similarity. All high energy peaks (Au4f$_{5/2}$) shift to ≈87.4 eV compared to the Au colloid grafted with MPA (86.7 eV) on the surface (see Figure S4, Supporting Information). This shift toward higher binding energy has already been described by VANEGAS et al.[39] and was attributed to the attachment of the ions to the nanoparticle surface (accompanied by ligand release).

If one compares the O1s signals induced by the carboxyl group of the MPA ligands at Au network surfaces, differences for bivalent ion-gelled samples can be observed compared to trivalent ion-gelled samples. In case of Ba^{2+} and Ca^{2+}, the observed two signals at 530.5 and 532.4 eV can most likely be attributed to the C=O group and the C–OH group of MPA, respectively, both interacting with the bivalent ions located between the C–OH group and the Au surface, as was already been observed by SHAMBETOVA et al.[36] These two peaks are not visible for the trivalent cation-gelled samples. Instead, the single maximum at 532 eV implies an interaction of the trivalent ions with the carboxyl group.

In conclusion, for pure gold gels, there is a structural influence of ion valences on the resulting nanoparticle network. The XPS results show that interactions between the ions present on the gold surface after gelation take place.

For NR gels induced by bivalent cations, the position of O1s signals is slightly different to those gelled by trivalent cation samples (Ba and Ca both at 531.1 eV, Y and Yb at 531.7 and 531.6 eV, respectively). We deduce that bivalent cations have been mostly eliminated from the gel networks by the washing process, since the signal for these elements (Ba, Ca) is missing in XPS and SEM-EDXS measurements (Figures 3; Figure S29, Supporting Information). Additionally, we performed ICP-OES measurements (see Figure S9, Supporting Information) on pure NR aerogels and supernatants from the hydrogels after 24 h of aging. We observe a significant difference between bi- and trivalent ions in terms of their concentration in the aerogels (being thoroughly washed and supercritically dried) and the pristine supernatant above the hydrogels. While the majority of the loosely bound bivalent cations is eliminated from the surface (proven by their low amount in aerogels), trivalent ions remain in the sample even after transferring the gels to dry acetone and performing the supercritical drying. This suggests the lack of interaction between the NR surface and the bivalent ions.

Nevertheless, the O1s signal shows an interaction with all cationic species with the carboxyl group, since only one maximum is observed in each measurement (in absence of cations, two maxima would be expected, one for the C=O and one for the OH group, respectively). This means that indeed there are cations present around the ligand shells of the particles. In the case of bivalent cations, however, they are not directly detectable. We explain the missing direct detectability in the following way: The gelation process removes ligands from the nanocrystal surface.[27] Thus, there are very few ligands left in the purified network to which cations can potentially be attached. This is likely the reason for the number of cations on MPA ligands being below the detection limit of the elements in both XPS and SEM-EDXS, and therefore no direct detection of the elements is possible. Instead, for trivalent cations, this behavior is slightly different: The O1s signal is slightly shifted towards higher binding energies for gels containing Y^{3+} and Yb^{3+} ions. Furthermore, the XPS and SEM-EDXS results show that a considerable (small) amount of trivalent cations remains even after washing, so that some degree of electrostatic interaction between the ligands and the ions (in addition to the accumulation of ions on the NR surface) cannot be completely excluded. For the interpretation of the detailed interaction between ions and particle surfaces during the network formation and washing process, further studies need to be carried out in future.

Focusing on the S2p signal in the pure NR samples (gelled with all investigated ions: Ba^{2+}, Ca^{2+}, Y^{3+}, and Yb^{3+} from the corresponding chlorides), one can observe differences in the lower energy range (160–161 eV). The two signals in the higher energy range are correlated with oxidized sulfur species (thiolated ligands or CdS surface), most likely due to the environmental conditions during sample preparation leading to partial oxidation of the sulfur species. Similar surface oxidation has already been found in comparable systems.[27] Regarding the low-energy part of the spectrum, in the case of CdSe/CdS gelled with Y^{3+} ions, the signal at 158.5 eV can be attributed to the contribution of the Y3d$_{3/2}$ orbital.[40] The signals at 160.6 eV (CdSe/CdS with Y^{3+}) and 160.9 eV (CdSe/CdS with Yb^{3+}) correspond to the interaction between sulfur and the trivalent ions,[41] which is a clear indication for the presence of trivalent ions on the nanoparticle surfaces in both cases. A significant difference between trivalent ion-gelled and bivalent ion-gelled samples is that this contribution is not found in the gels prepared with the bivalent ones Ba^{2+} and Ca^{2+} ions.

In summary for the XPS analysis for pure nanorod gels, it is found that in all cases there is an interaction between the carboxyl group of the MPA and the respective ions (Ba^{2+}, Ca^{2+}, Y^{3+}, and Yb^{3+}). In the case of trivalent ions, an additional interaction between the ions (Y^{3+} and Yb^{3+}) and the nanorod surface can be identified implying a more pronounced ligand release for such cations.

In total, the XPS measurements support our proposed gelation mechanisms for different cations, where bivalent ionic species can interact with the carboxylic acid of MPA and are not found on the surface of the semiconductor but on the surface of Au (due to a complex interaction between the gold surface, carboxyl group and the bivalent cations). Trivalent ionic species can be found both i) at the surface of NRs and Au within the network structures and ii) at the remaining MPA ligands.

Charge carrier dynamics can be altered via mixing the semiconductor NRs with Au NP, hence, the effect of the noble metal nanoparticle content on the PL properties of the NR backbone was investigated. Monitoring the radiative optical processes via photoluminescence quantum yield (PLQY) and time-resolved
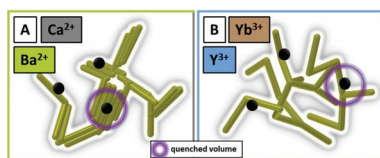
Scheme 2. Schematic representation of NR gel networks containing Au NP (namely heteroassemblies). A) Network obtained from bivalent cations (Ca^{2+}, Ba^{2+}), B) network obtained from trivalent cations (Y^{3+}, Yb^{3+}). More NRs are in the vicinity of Au NP to get quenched.

photoluminescence lifetime (FLT) measurements of colloidal mixtures, hydrogels, and their corresponding aerogels indicates gelation agent-dependent changes in the charge carrier dynamics. Figure 2 includes PLQY (panels A–C) values and the average PL lifetimes (Figure 2D–F) of the mixed systems using CdSe/CdS NRs and Au NPs (see Figure S11, Supporting Information, for the CdSe/CdS:Pt mixed systems). Experimental FLT decay curves can be found in the supporting information, see Figures S5, S14, S15, and S18 (Supporting Information) for colloidal mixtures, hydrogels, and aerogels.

The colloidal mixtures, which follow a gradual quenching of PLQY with increasing amount of noble metal NPs, contain electrostatically stabilizing surface ligands, which prevent the charge carrier exchange from particle to particle. These findings are discussed in detail in our previous publication about fluorescence quenching in mixed semiconductor noble metal networks.[31] For mixed colloidal solutions, the observed decrease of the PLQY is a consequence of the increased absorption of Au NPs in the UV–vis region (Figure 2A).

In contrast, hydrogels and aerogels show more pronounced quenching upon increasing the Au NP content in the heteroassemblies (NR:NP). It is important to emphasize that the samples prepared by a certain valency of ion behave in the same manner for the investigated ions. We assume that regardless of the density of the material, the excited electrons can only travel over a certain distance within the interconnected semiconductor network. In other words, a larger number of nanorods can be quenched within a denser network, which are produced by bivalent ions. **Scheme 2** visualizes the proposed dependency of the nanorod quantity in the quenched volume within the NR networks. The Au NP present have the greatest effect on the quenching of the fluorescence in the semiconductor network gelled with bivalent cationic species (Ba^{2+} and Ca^{2+}). The photoluminescence quantum yields of the networks gelled with trivalent ions show a steady decrease to almost 0 % PLQY. In the case of networks gelled with bivalent ions, this effect is much more pronounced for both hydrogels and aerogels visible as a stronger decrease for lower amount of Au NP. In aerogels (Figure 2C,F), however, the absolute PLQY values of bivalent ion-induced systems increase with respect to the corresponding hydrogels. Although we have observed increase of the PLQY of NRs aerogels compared to the respective hydrogels (gelled via hydrogen peroxide) upon supercritical drying previously,[5] this effect is not yet completely understood and might be of different origin, here. The ligand release (and subsequent roughness, see Figure 1) induced by the trivalent cations might generate trap states on the NR surface which further quenches the PL in network samples. This is in line with our previous findings

upon gelling CdSe/CdS NRs with less amount of Y^{3+} and Yb^{3+} cations, where the PLQY was highly enhanced when the NRs surface remained smooth.[27] This underlines the difference of the chemical environments as well as the different sample treatments for hydrogels and aerogels. To obtain aerogels, hydrogels are additionally washed with anhydrous acetone ensuring the compatibility of the samples with the supercritical drying. In this process, the inner pore solvent is exchanged from acetone to liquid CO_2 and afterwards to air. While the aerogelation itself does not change the PLQY values of the trivalent cation-gelled networks, the quantum yields increase from hydrogels to aerogels upon using bivalent cations. This suggest a more sensitive charge carrier recombination process to the chemical environmental changes: i) the relative permittivity of the solvent in the gap between the Au NPs and the CdSe/CdS NRs backbone decreases drastically in the aerogelation process, which might hinder the charge carrier transfer toward the quenching centers (e. g., trap states) leading to higher PLQY values. ii) The solvent effect seems to influence the interparticle connections within the side-by-side connected NR clusters and might eliminate solvent-related quenching effects in the aerogels.

FLT values for hydrogels and aerogels (for experimental decay curves see Figure S14, S15, and S18, Supporting Information) were calculated with amplitude weighted averaging of the biexponential fitting components. Gel networks obtained from bivalent ions tend to have biexponential decay curves while those from trivalent ions show a more monoexponential behavior which cannot be completely explained at present. PLQY and FLT values indicate a rather homogeneous quenching for the trivalent cation-gelled networks, but a rather inhomogeneous quenching for the gels prepared by bivalent cations seen in the biexponential decay (see Figure S14, Supporting Information). This inhomogenious quenching implies an additional nonradiative pathway coming from the interaction between semiconductor NRs and the noble metal NPs. In hydrogels, the possible distance between NR network and Au NP can be overcome by conductivity of solvent molecules (we studied in more detail in our previous publication).[31] Drying of hydrogels in supercritical conditions to aerogels leads to significantly changed FLT values but solely for bivalent ion-induced gelation. It can be anticipated that this observation can be explained similarly to the PLQY values above. Additionally, during supercritical drying, high pressure is applied to the gel networks. The possible effect of pressure-induced decrease of the particle distance is more pronounced in networks which are gelled with bivalent ions resulting in a more effective charge carrier transport to Au NP (and Pt NP, see Supporting Information) in case of mixed NR:NP systems.

3. Conclusion

In this work, the effect of bivalent and trivalent cations as gelation agents on the structural and optical properties of various gel networks is revealed. The straightforward and easy-to-adapt method to control the morphology of homoparticle assemblies and mixed semiconductor and noble metal gel networks is based on the valency of the gelation ions. Derived from comprehensive XPS measurements, it is proposed that two

different gelation mechanisms govern the properties of the gel structures: while Ba^{2+} and Ca^{2+} electrostatically screen the charged surface ligands presumably at the side region of the NRs, Y^{3+} and Yb^{3+} attach to the nanoparticle surface and facilitate the partial release of the thiolated ligands preferentially at the tips.[27] This leads to a more compact, less porous gel network consisting of side-by-side connected NRs for bivalent cations, and hyperbranched, highly porous gel backbone with tip-to-tip connected building blocks for trivalent ions. Upon introducing Au NP to the homoparticle assembly (before gelation) with CdSe/CdS, heteroassemblies can be prepared with high Au (and Pt) loading and preserved morphology of the original semiconductor backbone. The structural variety has a direct impact on the optical properties and alters the photoluminescence quantum yields and lifetimes. While a more inhomogenous quenching can be observed in the bivalent ion-induced networks, trivalent cations trigger the formation of gels being more homogeneous in terms of structural properties as well as PL quenching. In-depth optical studies indicate that photogenerated charge carriers can be spatially separated in all these heteroassemblies (in the form of hydro- as well as aerogels) which makes these structures a promising candidate for future applications in photocatalysis and sensing.

4. Experimental Section

Chemicals: Tri-*n*-octylphosphine oxide (TOPO, 99 %), sulphur (S, 99.98 %), 1,2,3,4-tetrahydronaphthalene (tetraline, 99 %), oleylamine (OAm, 70 %), 1-octadecene (ODE, 90 %), 3-mercaptopropionic acid (MPA, 99 %), ytterbium(III) chloride hexahydrate (Yb^{3+}, 99.9 %), yttrium(III) chloride hexahydrate (Y^{3+}, 99.99 %), barium chloride dihydrate (Ba^{2+}, 99 %), sodium borohydride (NaBH$_4$, 99 %), ethanol absolute (99.8 %), acetone (99.5 %) and methanol (99.8 %) were purchased from Sigma–Aldrich. Tri-*n*-octylphosphine (TOP, 97 %), dihydrogen hexachloroplatinate hexahydrate (H$_2$PtCl$_6$ · 6H$_2$O, 99.99 %), trisodium citrate dihydrate (Na-Citrate, 99 %) were purchased from ABCR. Cadmium oxide (CdO), hydrogen tetrachloroaurate(III) trihydrate (HAuCl$_4$ · 3H$_2$O, 99.99 %), borane tert-butylamine complex (TBAB, 97 %), selenium (Se, 99.99 %) were purchased from Alfa Aesar. Hexylphosphonic acid (HPA, 99 %), octadecylphosphonic acid (ODPA, 99 %) were purchased from PCI Synthesis. Toluene (99.9 %) was purchased from Merck Millipore. Calcium chloride (Ca^{2+}, 98 %) was purchased from Roth. Acetone extra dry (99.8 %) was purchased from Acros. All chemicals were used as purchased and without further purification.

Synthesis of CdSe Seeds: CdSe seeds were prepared according to Carbone et~al.[42] In a typical synthesis, CdO (0.06 g, 0.47 mmol), ODPA (0.28 g, 0.84 mmol) and TOPO (3.0 g, 7.76 mmol) were mixed in a 25 mL flask and in vacuum heated to 150 °C. After 1 h, the atmosphere was switched to argon and the flask was heated to 300 °C for dissolving the CdO until a clear solution was obtained. TOP (1.8 mL, 4.04 mmol) were added, and the flask was heated to 380 °C. At this temperature a mixture of TOP (1.8 mL, 4.04 mmol) and Se (0.058 g, 0.73 mmol) was injected in the flask.

The reaction was quenched after 4 min by the injection of ODE (4 ml) and the removal of the heating mantle. The flask was cooled down to 90 °C and toluene (5 mL) was added. For purification, the particles were precipitated with methanol (8 mL), centrifuged (10 min., 8000 rcf) and redissolved in hexane (8 mL). This step was repeated twice and the particles were finally stored in hexane (2 mL).

CdSe/CdS dot-in-rod Particles: This synthesis was carried out by a seeded-growth method.[42] CdO (0.06 g, 0.47 mmol), HPA (0.08 g, 0.48 mmol), ODPA (0.28 g, 0.84 mmol) and TOPO (9 g, 23.28 mmol)

were mixed in a flask and heated up to 150 °C for 1 h in vacuum. After degassing the atmosphere were switched to argon and the reaction solution was heated to 300 °C until a clear solution was obtained. TOP (1.8 mL, 4.04 mmol) was injected in the flask, and the synthesis solution was heated to 350 °C.

The prepared spherical CdSe nanoparticles (0.08 µmol) in hexane were dried with air flow and redissolved in a TOP:S mixture (1.8 mL, 4.04 mmol TOP and 0.13 g, 4.05 mmol S) in inert atmosphere. This mixture was quickly injected at 350 °C into the flask by which the temperature decreased to 285 °C. After reaching 350 °C reaction, the temperature was held for 8 min after injection and then air-cooled down to 90 °C, and toluene (5 mL) was injected.

The purification was carried out by alternating precipitation with methanol (4 mL), centrifugation at 3773 rcf and redispersion in toluene (4 mL) for at least three times. The final NR solution was stored in toluene (12 mL). The size of the NRs was measured by TEM from organic solution (preferably from chloroform).

Phase Transfer of CdSe/CdS Nanorods: The CdSe/CdS nanorods in organic solution were transferred into aqueous solution by ligand exchange.[43,44] For phase transfer, 12 mL of the nanoparticle solution was precipitated in a mixture of methanol (100 mL), MPA (2.6 mL, 29.84 mmol), and KOH (1.14 g, 20.32 mmol) and shaken for 2 h at room temperature in centrifugation vails.

After centrifugation (10 min., 8500 rcf), the precipitate was redispersed in 0.1 M aqueous KOH solution (30 mL). Concentration was determined by atom absorption spectroscopic measurements (AAS).

Synthesis of Au Nanoparticles: Synthesis of the spherical gold nanoparticles was carried out according to Peng et al.[45] HAuCl$_4$ · 3H$_2$O (0.1 g, 0.25 mmol), tetraline (10 mL), and OAm (10 mL) were mixed in a flask at room temperature and ambient conditions through stirring for 10 min. TBAB (34.48 mg, 0.40 mmol), OAm (1 mL), and tetraline (1 mL) were sonicated until the TBAB was dissolved. The TBAB solution was quickly injected into the flask, and the reactionsolution was stirred for 2 h at 44 °C. For purification, the nanoparticle solution was divided into two parts with a volume of 11 mL, and each sample was precipitated with ethanol (35 mL). After centrifugation (10 min, 8500 rcf), the precipitated nanoparticles were redispersed in toluene (5 mL).

Phase Transfer of Au Nanoparticles: For phase-transfer according to Hiramatsu et al.[46] of the as-prepared spherical nanoparticles, particles in toluene (4.5 mL) were added to a boiling solution of toluene (44 mg, 0.22 mmol nanoparticles in 90 mL toluene). By adding MPA (4.5 mL, 51.64 mmol) the nanoparticles were precipitated as a black solid. After centrifugation (10 min, rcf 8500), the particles were redispersed in 0.01 M KOH (5 mL) followed by precipitation with ethanol (10 mL). This purification step was repeated twice and the particles were finally stored in 0.01 M aqueous KOH solution (3 mL).

Synthesis of Pt Nanoparticles: Synthesis of spherical Pt nanoparticles was carried out in aqueous solution according to Bigall et al.[47] The synthesis was done four times and blend to one large batch. 36.2 mL of 0.2 % H$_2$PtCl$_6$ · 6H$_2$O solution was diluted with 464 mL boiling H$_2$O. At 100 °C, 11.6 mL of 1 % sodium citrate solution was added. After 60 s, we added 5.5 mL of a freshly prepared NaBH$_4$ solution. The NaBH$_4$ solution was prepared from 50 mL ice-cold H$_2$O, 0.038 g NaBH$_4$, and 0.5 g sodium citrate. The solution turned immediately into a grayish solution, which was held for 10 minu at the boiling temperature. The solution was cooled down to room temperature and collected together with all other batches.

Purification and Concentrating of Pt Nanoparticle Solution: Multiple Pt synthesis solutions were filtered with an ultrafiltration cell at high pressure. Filtering sheets with a MWCO of 10 000 PES were used to separate particles from the surrounding aqueous solution. 2 L assynthesized Pt nanoparticles were concentrated to ≈50–100 mL solution. In the next step, the Pt solution was washed and concentrated with centrifuge filters (Amicron Ultra-15, MWCO 30,000). Here, sample amounts of 12 mL were reduced to 2 mL step by step, until the whole solution was reduced to ≈12 mL. These 12 mL were washed with pure deionized water 10 times with centrifuge filters. The resulting solution was filtered by syringe filters and fixed to 10.5 mL with deionized water.

Ligand Exchange of Pt Nanoparticles: Ligand exchange from citrate to mercaptopropionic acid (MPA) was carried out by the following procedure. A phase transfer solution was prepared from 15 mL methanol, 0.32 g KOH and 776 μL MPA. The solution was sonicated in an ultrasonic bath until KOH was completely dissolved. Six milliliter of freshly prepared phase transfer solution was mixed with 2 mL of the as prepared and cleaned Pt solution and shaken for 5 h. The solution was centrifuged (10 min, rcf 5000) and the particles were dissolved in 0.01 M KOH. The final concentration of Pt nanoparticles was 10.4 g L^{-1}.

Preparation of Hydrogels: Colloidal solutions were mixed according to the calculated particle ratios by keeping the Cd concentration constant (3.6 mg mL^{-1}, determined from AAS, see below). For example CdSe/CdS:Au 5:1 was prepared by mixing 74.9 μL (0.18 mM Cd) CdSe/CdS and 4.4 μL (54 μM Au) Au colloidal solution in a small Eppendorf recation tube together with 296 μL 0.01 M KOH aqueous solution. The mixture was well shaken. After mixing, 42 μL of a 50 mM salt solution (of the respective salts BaCl$_2$ · 2H$_2$O, CaCl$_2$, YCl$_3$ · 6H$_2$O,[27] and YbCl$_3$ · 6H$_2$O[27]) was added to the samples, which were well shaken and stored at room temperature for 24 h for the aging process on a bench. Samples were washed several times with ultrapure water to reduce byproducts and KOH content. Washing was carried out by exchange of the supernatant above the network structure to ultra pure water for ten times. The supernatant was removed with a pipette above the hydrogel surface, and the Eppendorf reaction tube was carfully refilled with ultra pure water. Between two washing steps, there was a minimum of 1 h to ensure the solvent accessing the pores from the network. Purified samples were transferred carefully via pipettes to PMMA cuevettes for spectroscopic investigations.

Preparation of Aerogels: After washing ten times with water, solvents in hydrogel samples were exchanged to acetone until no more streaks were visible in the solvent. Solvent exchange to acetone was followed by extra dry acetone for five times with the same procedure like washing (see hydrogels). These acetogel samples were supercritically dried with liquid CO$_2$ inside a critical point dryer (SPI-DRY). This procedure was carried out by cutting the Eppendorf reaction tubes above the sample. In a transfer vessel from the critical point dryer filled with dried acetone, the samples in the cutted tubes were placed inside the autoclave. The liquid acetone was exchanged to liquid CO$_2$ and flushed for 4 to 5 min. The sample was left over night within the autoclave and flushed again with liquid CO$_2$ the next day for 5 min. For the drying process, liquid CO$_2$ was heated to ≈36 °C to reach the supercritical point at 31 °C and 74 bar. Aerogel samples were taken out of the autoclave stored in ambient conditions before measurements took place.

Transmission Electron Microscopy (TEM): Samples were prepared on carbon coated copper grids (300 mesh, Quantifoil). Nanoparticle (except Pt, which is prepared from water) solutions were drop-casted from non-polar solvents (preferably from CHCl$_3$) gel network structures were prepared from hydro- and aerogels. For hydrogels, fragments of the network structures were drop-casted on the grid. Aerogels were touched by the copper grids to collect gel fragments. The measurement was performed with a FEI Tecnai G2 F20 TMP microscope operated at 200 kV.

Scanning Electron Microscopy (SEM): Aceto- and aerogels were glued on carbon infiltrated conductive polymer from Plano. SEM images were taken with a JEOL JSM-6700F operated at 2 kV using secondary electron signal. Using an Oxford Instruments INCA 300 EDXS, elemental analysis was made with 10 kV accelerating voltage.

XPS Measurements: XPS measurements were performed on a PHI VersaProbe III with an Al 1486.6 eV mono at 25.2 W Xray source. Pass energies of 224 eV (increment of -0.2 eV, 0.2 s per data point) for survey spectra and 27 eV (increment of -0.05 eV, 2.4 s per data point) for high-resolution spectra of defined energy regions for different elements were taken. The measurement was done with a beam diameter of 100 μm. Samples were neutralized during the measurement with 1 V and 3 μA. All samples were dropcasted on Si-wafers and charge corrected with the C1s signal for C–C binding at 284.8 eV. Raw data were fitted and evaluated with MultiPak and Shirley baseline correction.

Optical Spectroscopy: Fluorescence lifetime measurements (time correlated single photon counting - TCSPC) were carried out with an Edinburgh FLS 1000 spectrofluorometer irradiated with a 445.1 nm laser LED (2 ms repetition rate) and measured at the maximum emission wavelength of the samples. Decay curves were fitted with exponential fit and amplitude weighted in case of biexponential curves. Emission spectra and photoluminescence quantum yields in absolute mode were measured in an integrating sphere attached to the same spectrofluorometer with an excitation wavelength of 445.1 nm. Excitation slits (1 nm) and emission slits (0.6 nm) were constant for all measurements. Moreover, absorption spectra for colloidal mixtures, hydrogels and aerogels were measured with an Agilent Cary 500 in an integrating sphere with a spectral resolution of 1 nm without filters.

Atom Absorption Spectroscopy (AAS): To determine the particle concentrations, AAS spectroscopy was performed with a VARIAN AA140 in acetylene/air flame at element specific wavelength (at Au 242.8 nm, Cd 228.8 nm and Pt 266 nm).

Supporting Information

Supporting Information is available from the Wiley Online Library or from the author.

Acknowledgements

Conflict of Interest

The authors declare no conflict of interest.

Data Availability Statement

The data that support the findings of this study are available from the corresponding author upon reasonable request.

Keywords

[1] J. Wang, *Anal. Chim. Acta* **2003**, *500*, 247.

[2] J. L. Mohanan, S. L. Brock, *J. Non-Cryst. Solids* **2004**, *350*, 1.

[3] J. L. Mohanan, I. U. Arachchige, S. L. Brock, *Science* **2005**, *307*, 397.

[4] I. U. Arachchige, S. L. Brock, *J. Am. Chem. Soc.* **2007**, *129*, 1840.

[5] S. Sanchez-Paradinas, D. Dorfs, S. Friebe, A. Freytag, A. Wolf, N. C. Bigall, *Adv. Mater.* **2015**, *27*, 6152.

[6] B. Cai, V. Sayevich, N. Gaponik, A. Eychmüller, *Adv. Mater.* **2018**, *30*, 1707518.

[7] A. Figuerola, I. R. Franchini, A. Fiore, R. Mastria, A. Falqui, G. Bertoni, S. Bals, G. Van Tendeloo, S. Kudera, R. Cingolani, L. Manna, *Adv. Mater.* **2009**, *21*, 550.

[8] S. K. Gill, L. J. Hope-Weeks, *Chem. Commun.* **2009**, *29*, 4384.

[9] S. K. Gill, P. Brown, L. J. Hope-Weeks, *J. Sol-Gel Sci. Technol.* **2011**, *57*, 68.

[10] P. Li, A. Lappas, R. Lavieville, Y. Zhang, R. Krahne, *J. Nanopart. Res.* **2012**, *14*, 978.

[11] T. Hendel, V. Lesnyak, L. Kühn, A.-K. Herrmann, N. C. Bigall, L. Borchardt, S. Kaskel, N. Gaponik, A. Eychmüller, *Adv. Funct. Mater.* **2013**, *23*, 1903.

[12] L. Nahar, R. J. A. Esteves, S. Hafiz, U. Oezguer, I. U. Arachchige, *ACS Nano* **2015**, *9*, 9810.

[13] R. Wendt, B. Märker, A. Dubavik, A.-K. Herrmann, M. Wollgarten, Y. P. Rakovich, A. Eychmüller, K. Rademann, T. Hendel, *J. Mater. Chem. C* **2017**, *5*, 10251.

[14] J. L. Davis, K. L. Silva, S. L. Brock, *Chem. Commun.* **2020**, *56*, 458.

[15] D. Zámbó, A. Schlosser, R. T. Graf, P. Rusch, P. A. Kißling, A. Feldhoff, N. C. Bigall, *Adv. Opt. Mater.* **2021**, *9*, 2100291.

[16] A. Schlosser, L. C. Meyer, F. Lübkemann, J. F. Miethe, N. C. Bigall, *Phys. Chem. Chem. Phys.* **2019**, *21*, 9002.

[17] X. Luo, A. Morrin, A. Killard, M. Smyth, *Electroanalysis* **2006**, *18*, 319.

[18] Q. Yao, S. L. Brock, *Nanotechnology* **2010**, *21*, 115502.

[19] W. Liu, A.-K. Herrmann, D. Geiger, L. Borchardt, F. Simon, S. Kaskel, N. Gaponik, A. Eychmüller, *Angew. Chem., Int. Ed.* **2012**, *51*, 5743.

[20] L. Korala, J. R. Germain, E. Chen, I. R. Pala, D. Li, S. L. Brock, *Inorg. Chem. Front.* **2017**, *4*, 1451.

[21] S. Sekiguchi, K. Niikura, N. Iyo, Y. Matsuo, A. Eguchi, T. Nakabayashi, N. Ohta, K. Ijiro, *ACS Appl. Mater. Interfaces* **2011**, *3*, 4169.

[22] F. Matter, A. L. Luna, M. Niederberger, *Nano Today* **2020**, *30*, 100827.

[23] A. Freytag, S. Sánchez-Paradinas, S. Naskar, N. Wendt, M. Colombo, G. Pugliese, J. Poppe, C. Demirci, I. Kretschmer, D. W. Bahnemann, P. Behrens, N. C. Bigall, *Angew. Chem., Int. Ed.* **2016**, *55*, 1200.

[24] D. Müller, D. Zámbó, D. Dorfs, N. C. Bigall, *Small* **2021**, *17*, 18.

[25] V. Lesnyak, A. Wolf, A. Dubavik, L. Borchardt, S. V. Voitekhovich, N. Gaponik, S. Kaskel, A. Eychmüller, *J. Am. Chem. Soc.* **2011**, *133*, 13413.

[26] R. Du, Y. Hu, R. Hübner, J.-O. Joswig, X. Fan, K. Schneider, A. Eychmüller, *Sci. Adv.* **2019**, *5*, eaaw4590.

[27] D. Zámbó, A. Schlosser, P. Rusch, F. Lübkemann, J. Koch, H. Pfnür, N. C. Bigall, *Small* **2020**, *16*, 1906934.

[28] L. Altenschmidt, S. Sánchez-Paradinas, F. Lübkemann, D. Zámbó, A. M. Abdelmonem, H. Bradtmüller, A. Masood, I. Morales, P. de la Presa, A. Knebel, M. A. G. García-Tuñón, B. Pelaz, K. D. Hindricks, P. Behrens, W. J. Parak, N. C. Bigall, *ACS Appl. Nano Mater.* **2021**, *4*, 6678.

[29] N. Gaponik, A. Wolf, R. Marx, V. Lesnyak, K. Schilling, A. Eychmüller, *Adv. Mater.* **2008**, *20*, 4257.

[30] P. Rusch, D. Zámbó, N. C. Bigall, *Acc. Chem. Res.* **2020**, *53*, 2414.

[31] M. Rosebrock, D. Zámbó, P. Rusch, D. Pluta, F. Steinbach, P. Bessel, A. Schlosser, A. Feldhoff, K. D. J. Hindricks, P. Behrens, D. Dorfs, N. C. Bigall, *Adv. Funct. Mater.* **2021**, *31*, 2101628.

[32] J. Schlenkrich, D. Zámbó, A. Schlosser, P. Rusch, N. C. Bigall, *Adv. Opt. Mater.* **2022**, *10*, 2101712.

[33] A. Schlosser, J. Schlenkrich, D. Zámbó, M. Rosebrock, R. T. Graf, G. Escobar Cano, N. C. Bigall, *Adv. Mater. Interfaces* **2022**, *9*, 2200055.

[34] D. Wen, A. K. Herrmann, L. Borchardt, F. Simon, W. Liu, S. Kaskel, A. Eychmüller, *J. Am. Chem. Soc.* **2014**, *136*, 2727.

[35] P. Rusch, B. Schremmer, C. Strelow, A. Mews, D. Dorfs, N. C. Bigall, *J. Phys. Chem. Lett.* **2019**, *10*, 7804.

[36] N. Shambetova, Y. Chen, H. Xu, L. Li, J. Solandt, Y. Zhou, J. Wang, H. Su, H. Brismar, Y. Fu, *J. Phys. Chem. C* **2016**, *120*, 3519.

[37] S. Deka, A. Falqui, G. Bertoni, C. Sangregorio, G. Poneti, G. Morello, M. D. Giorgi, C. Giannini, R. Cingolani, L. Manna, P. D. Cozzoli, *J. Am. Chem. Soc.* **2009**, *131*, 12817.

[38] T. Mokari, E. Rothenberg, I. Popov, R. Costi, U. Banin, *Science* **2004**, *304*, 1787.

[39] J. P. Vanegas, J. C. Scaiano, A. E. Lanterna, *Langmuir* **2017**, *33*, 12149.

[40] D. Majumdar, D. Chatterjee, *J. Appl. Phys.* **1991**, *70*, 988.

[41] R. P. Vasquez, *J. Electron Spectrosc. Relat. Phenom.* **1990**, *50*, 167.

[42] L. Carbone, C. Nobile, M. De Giorgi, F. D. Sala, G. Morello, P. Pompa, M. Hytch, E. Snoeck, A. Fiore, I. R. Franchini, M. Nadasan, A. F. Silvestre, L. Chiodo, S. Kudera, R. Cingolani, R. Krahne, L. Manna, *Nano Lett.* **2007**, *7*, 2942.

[43] H. G. Bagaria, E. T. Ada, M. Shamsuzzoha, D. E. Nikles, D. T. Johnson, *Langmuir* **2006**, *22*, 7732.

[44] T. Kodanek, H. M. Banbela, S. Naskar, P. Adel, N. C. Bigall, D. Dorfs, *Nanoscale* **2015**, *7*, 19300.

[45] S. Peng, Y. Lee, C. Wang, H. Yin, S. Dai, S. Sun, *Nano Res.* **2008**, *1*, 229.

[46] H. Hiramatsu, F. E. Osterloh, *Chem. Mater.* **2004**, *16*, 2509.

[47] N. Bigall, A.-K. Herrmann, M. Vogel, M. Rose, P. Simon, W. Carrillo-Cabrera, D. Dorfs, S. Kaskel, N. Gaponik, A. Eychmüller, *Angew. Chem., Int. Ed.* **2009**, *48*, 9731.

2206818 (11 of 11)